inorganics

MDPI

Article

Preparation of Non-Noble Metal Catalyst $FeCo_2O_4/MoS_2$ for Production of Hydrogen and Oxygen by Electrochemical Decomposition of Water

Zhouqian Chen [1,2,†], Zongmei Li [1,†], Manyi Zhang [3], Yujia Wang [4], Siang Zhang [2] and Yuanyuan Cheng [1,*]

[1] School of Science, China University of Geosciences (Beijing), Beijing 100083, China; valeriacc@163.com (Z.C.); lizongmei2024@163.com (Z.L.)
[2] School of Earth Sciences and Resources, China University of Geosciences (Beijing), Beijing 100083, China; 15210852692@163.com
[3] School of Foreign Languages, China University of Geosciences (Beijing), Beijing 100083, China; ha1689yayaha@163.com
[4] School of Economics and Management, China University of Geosciences (Beijing), Beijing 100083, China; wangyujia820@gmail.com
* Correspondence: yycheng@cugb.edu.cn
† These authors contributed equally to this work.

Abstract: $FeCo_2O_4/MoS_2$ binary composite catalysts were prepared by the hydrothermal method and calcination method. In this paper, the morphology and structure of the materials were characterized by means of SEM, EDS, XRD, and XPS. It was found that MoS_2 has high activity and good stability in HER, and and it has more prospect than noble metal catalysts. In oxygen evolution chemical kinetics, its rich redox potential allowed it to adsorb OH^- on (Co^{2+}/Co^{3+}, Fe^{2+}/Fe^{3+}) and enhanced the activity of OER. The cross-nanosheet structure of the $FeCo_2O_4/MoS_2$ composite catalyst exposed more catalytic sites and accelerated charge transfer to achieve more efficient mass transfer. $FeCo_2O_4/MoS_2$ as an anode and cathode was assembled into a two-electrode system in overall water splitting, which showed good catalytic activity. When the composite ratio of $FeCo_2O_4$ to MoS_2 was 1:0.3, the composite catalyst had the best catalytic activity. The results show that when $FeCo_2O_4/MoS_2$ is used as a cathode and anode to assemble an alkaline cell, respectively, the voltage for total water electrolysis is 1.59 V at a current density of 10 mA cm^{-2} in a 1 M KOH electrolyte, it can keep good stability in a 10 h test with electrolyzed water, and its current retention rate is 98.5%.

Keywords: $FeCo_2O_4$; MoS_2; oxygen evolution reaction; hydrogen evolution reaction; electrochemical decomposition of water

check for updates

Citation: Chen, Z.; Li, Z.; Zhang, M.; Wang, Y.; Zhang, S.; Cheng, Y. Preparation of Non-Noble Metal Catalyst $FeCo_2O_4/MoS_2$ for Production of Hydrogen and Oxygen by Electrochemical Decomposition of Water. *Inorganics* **2024**, *12*, 229. https://doi.org/10.3390/inorganics12080229

Academic Editor: Hicham Idriss

Received: 21 March 2024
Revised: 11 August 2024
Accepted: 14 August 2024
Published: 22 August 2024

1. Introduction

With the rapid development of society and the swift growth of the population, the demand for energy has been increasing significantly. It is estimated that approximately 80% of the world's energy primarily relies on the combustion of fossil fuels such as coal, oil, and natural gas, while only 20% of renewable energy sources (such as wind, tidal, and solar energy) are utilized [1,2]. However, the extensive burning of fossil fuels not only leads to the rapid depletion of energy resources but also causes serious environmental issues (such as global warming). Therefore, there is an urgent need to develop clean, sustainable, and renewable energy sources for long-term sustainable development. Since John Bockris proposed the concept of the hydrogen economy in the 1970s, hydrogen has been considered one of the cleanest and most promising sources of energy [3]. This is because the combustion product of hydrogen is only water, and it has a higher energy density than gasoline (120 MJ kg^{-1} vs. 44 MJ kg^{-1}), along with the advantage of zero carbon emissions [4].

This study focuses on the electrochemical method of producing hydrogen and oxygen using transition metals and composite materials. Currently, the main technologies for hydrogen production primarily include coal gasification [5] and natural gas reforming [6], and so far, about 96% of the world's hydrogen is obtained by these two methods. However, these hydrogen production technologies are overly dependent on fossil fuels, producing CO, CO_2, and sulfur oxides during the hydrogen production process, and requiring harsh conditions (high temperature and pressure). Additionally, hydrogen can also be produced through methods such as metal hydride acid hydrolysis [7] and photochemical water splitting [8]. However, these methods have their limitations; for example, the starting materials for metal hydride acid hydrolysis generally have corrosiveness, and photochemical water splitting is the slowest hydrogen production method among all of them. Unlike other hydrogen production technologies, electrochemical water splitting is a highly pure (≈99.99%), environmentally friendly, sustainable, and efficient hydrogen production technology. Moreover, this technology can be easily combined with other renewable clean energy sources such as solar, wind, and tidal energy. This series of advantages makes it stand out among various hydrogen production technologies, making it the most promising hydrogen production technology at present.

Ru, Pt [9], and Ir, which have the highest conversion efficiency as electrode materials, are the most common noble metal oxides in the study of water electrolysis catalysts; they exhibit excellent performance, but they have some defects, namely that they are soluble in alkaline electrolytes [10] and expensive, which leads to high costs and means they cannot obtain the product of electrolytic water efficiently. Therefore, it is necessary to develop some non-precious metal materials to reduce the impact of these defects on the water electrolysis reaction. In recent years, carbon-based materials such as graphene [11,12], carbon nanotubes [13], and graphyne [14,15] have been widely applied in the research on electrocatalysts. Graphene, carbon nanotubes, and other carbon materials have extremely high carrier mobility, large specific surface area, high mechanical strength, and high thermal conductivity. In metal–organic framework (MOF) materials [16], metal centers and organic ligands are evenly distributed, forming rich internal channels, having a large specific surface area, and improving the utilization rate of active sites. Transition metal oxides, due to their low cost, adjustable structure, and stable performance, are widely used. Spinel-type oxides are widely used due to their outstanding catalytic activity [17]. Transition metal-based electrocatalysts, such as transition metal oxides for OER [18,19] and sulfides for HER [20,21], have been extensively studied and achieved good results. However, the complex electron transfer process of OER and HER makes it a challenge for HER and OER catalysts to carry out overall electrochemical water splitting.

In the process of electrochemical water splitting, the complex coupling of multiple protons and electrons complicates the oxidation reaction (OER) and reduction reaction (HER), causing the reaction kinetics to be slow and requiring higher overpotentials to initiate the reaction. Nickel cobaltite ($NiCo_2O_4$) and iron cobaltite ($FeCo_2O_4$) and other bimetallic transition metal oxides, with their cost-effectiveness, simple preparation methods, and environmental friendliness, as well as their rich redox pair characteristics, become effective catalytic centers in OER. MoS_2, with its graphene-like layered structure, rivals precious metals like Pt in hydrogen adsorption energy, showing great potential as an HER catalyst. Studies have shown that coupling these bimetallic oxides with MoS_2 to construct heterojunction structures can enhance the intrinsic electrical conductivity and increase the number of active sites, thereby accelerating charge transfer and effectively enhancing catalytic efficiency. Due to their significant catalytic performance advantages, these materials are urgently needed. Simultaneously, the transition metal oxide selected in this study, ferric cobalt oxide ($FeCo_2O_4$), engages in redox reactions through a rich array of electron pairs (Fe^{2+}/Fe^{3+}, Co^{2+}/Co^{3+}), offering advantages such as low cost, minimal environmental pollution, and high reaction efficiency.

Extensive research indicates that transition metal compounds based on Fe and Co can expose more d-orbital electrons [22], thereby enhancing electrocatalytic activity and

showing great potential in catalyzing oxygen evolution reactions. Transition metal mixed oxides with spinel structures, such as cobalt spinel oxides, due to their high abundance, low cost, and adjustable structure/element performance, are considered the most promising water oxidation electrocatalysts in alkaline electrolytes. The metal ions at sites A and B providing multiple redox pairs are effective active centers for OER activity, and the unique structure of mixed valence cations enables electrons to transition at a low activation energy [23,24]. Molybdenum disulfide (MoS_2), a transition metal dichalcogenide, has recently attracted widespread attention. It has a graphene-like layered structure, composed of a single-layer S-Mo-S sandwich structure, connected by van der Waals forces. Depending on the stacking method, it can be divided into a tetragonal (1T) phase, hexagonal (2H) phase, and rhombohedral (3R) phase. The 1T phase exhibits metallic properties, and compared to 2H-MoS_2, has superior HER performance, with active sites distributed on both the edges and the basal plane [25–27]. A large body of research shows that MoS_2 has high activity and good stability in HER, promising to replace precious metal catalysts. Studies have found that through the synergistic effect between the two separate components, the electronic structure can be optimized, and the catalytic active sites regulated; hence, biphase composite catalysts have been extensively developed [28,29].

Herein, we prepared an $FeCo_2O_4/MoS_2$ composite catalyst to study its performance of water electrolysis. It was found that $FeCo_2O_4$ was synthesized by the hydrothermal method with $FeCl_3{\cdot}6H_2O$ and $CoCl_2{\cdot}6H_2O$, then an $FeCo_2O_4$ nanosheet was prepared by calcination at high temperature; the same method is used to make MoS_2 as well. At the end, an $FeCo_2O_4/MoS_2$ composite catalyst with a cross-structure was prepared by introducing a MoS_2 and $FeCo_2O_4$ nanosheet again by the hydrothermal method. When the composite ratio of $FeCo_2O_4$ and MoS_2 was 1:0.3, the composite catalyst had the best catalytic activity. At a current density of 10 mA cm^{-2}, it demonstrates good stability in water electrolysis.

2. Results and Discussion

2.1. SEM and EDS Analysis

The microstructure of the catalyst was characterized by scanning electron microscopy (SEM). As shown in Figure 1a,b, the synthesized $FeCo_2O_4$ and MoS_2 are both present in the form of nanosheets, and the sizes of the $FeCo_2O_4$ and MoS_2 nanoplates are about 2 μm and 100 nm, respectively. The morphology of the $FeCo_2O_4/MoS_2$ catalyst is shown in Figure 1c, where the $FeCo_2O_4$ and MoS_2 nanoplates can be seen crossing each other, which is beneficial for increasing the catalyst surface area and providing more active sites. Figure 1d shows the mapping image of the composite, which visually shows the presence of Fe, Co, Mo, O, and S elements in the $FeCo_2O_4/MoS_2$ composite catalyst. According to Figure 1, it can be found that Fe, Co, and O are distributed in the center of the composite catalyst, while Mo and S are distributed all over the catalyst, so it can be predicted that MoS_2 nanoplates physically accumulate on the substrate of $FeCo_2O_4$ nanoplates.

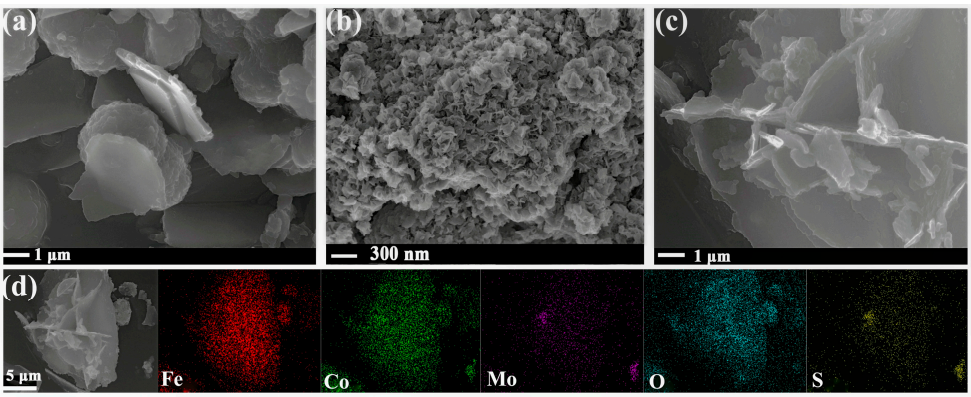

Figure 1. SEM images of catalysts: (**a**) $FeCo_2O_4$; (**b**) MoS_2; (**c**) $FeCo_2O_4/MoS_2$; (**d**) EDS map of $FeCo_2O_4/MoS_2$.

2.2. XRD Analysis

To make a further confirmation of the phase characterization of the catalyst, XRD characterization analysis was carried out. The powder XRD spectrum of FCO, MS, and FCO/MS-1 (catalyst samples) are shown in Figure 2. Peaks appearing at 31.294°, 36.874°, 44.844°, 59.404°, and 65.289° respectively belong to the (200), (311), (400), (511), and (440) crystal faces of spinel structure $FeCo_2O_4$ (JCPDS No.: 22-1086) [30], which is exactly the same as the data reported before [31,32]. In addition, the sharp diffraction peak of $FeCo_2O_4$ shows that the synthesized $FeCo_2O_4$ has good crystallinity. Peaks appearing at 14.391°, 32.803°, and 58.560° belong to the (002), (100), and (110) crystal faces of MoS_2. In the powder XRD spectrum of the composite material FCO/MS-1 (blue line), it can be observed intuitively that two peaks of different substances are contained in the composite structure, which could indicate success in preparing the $FeCo_2O_4/MoS_2$ composite catalyst combined with the analysis results of EDS.

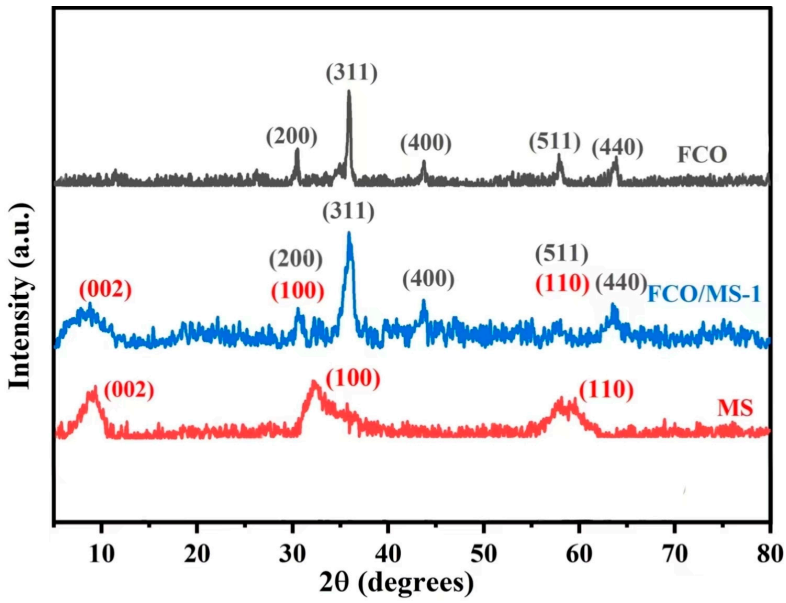

Figure 2. XRD patterns of FCO, MS, and FCO/MS-1 powder samples.

2.3. XPS Analysis

Adopting X-ray photoelectron spectroscopy (XPS), the chemical valence states of the synthesized FCO/MS-1 samples were characterized, and calibrated all the elements with the reference of C 1s (284.8 eV). Figure 3a shows the XPS results for FCO/MS-1, which clearly show the presence of the elements Fe, Co, Mo, S, and O in agreement with the EDS analysis.

Figure 3b shows the XPS spectrum of Fe 2p, which can be assigned to Fe 2p3/2 and Fe 2p1/2, respectively. The characteristic peaks at 717.9 and 723.7 eV are two satellite peaks of Fe, while the characteristic peaks at 710.3 and 723.6 eV can be attributed to Fe^{2+}, the other those which at 713.1 and 726.0 eV can be attributed to Fe^{3+} [32].

Figure 3c shows the XPS spectrum of Co 2p, which can be assigned to Co $2p_{3/2}$ and Co $2p_{1/2}$, respectively. The characteristic peaks at 779.7, 781.86, 795.0, and 796.8 eV can be attributed to the satellites of Co (III) $2p_{3/2}$, Co (II) $2p_{3/2}$, Co (III) $2p_{1/2}$, and Co (II) $2p_{1/2}$; the characteristic peaks at 786.3 and 802.6 eV are the satellite peaks of Co. These results indicate that cobalt is mainly present in divalent and trivalent forms, and the presence of multivalent cobalt and iron confirms that $FeCo_2O_4$ in the composite catalyst has a spinel structure [33].

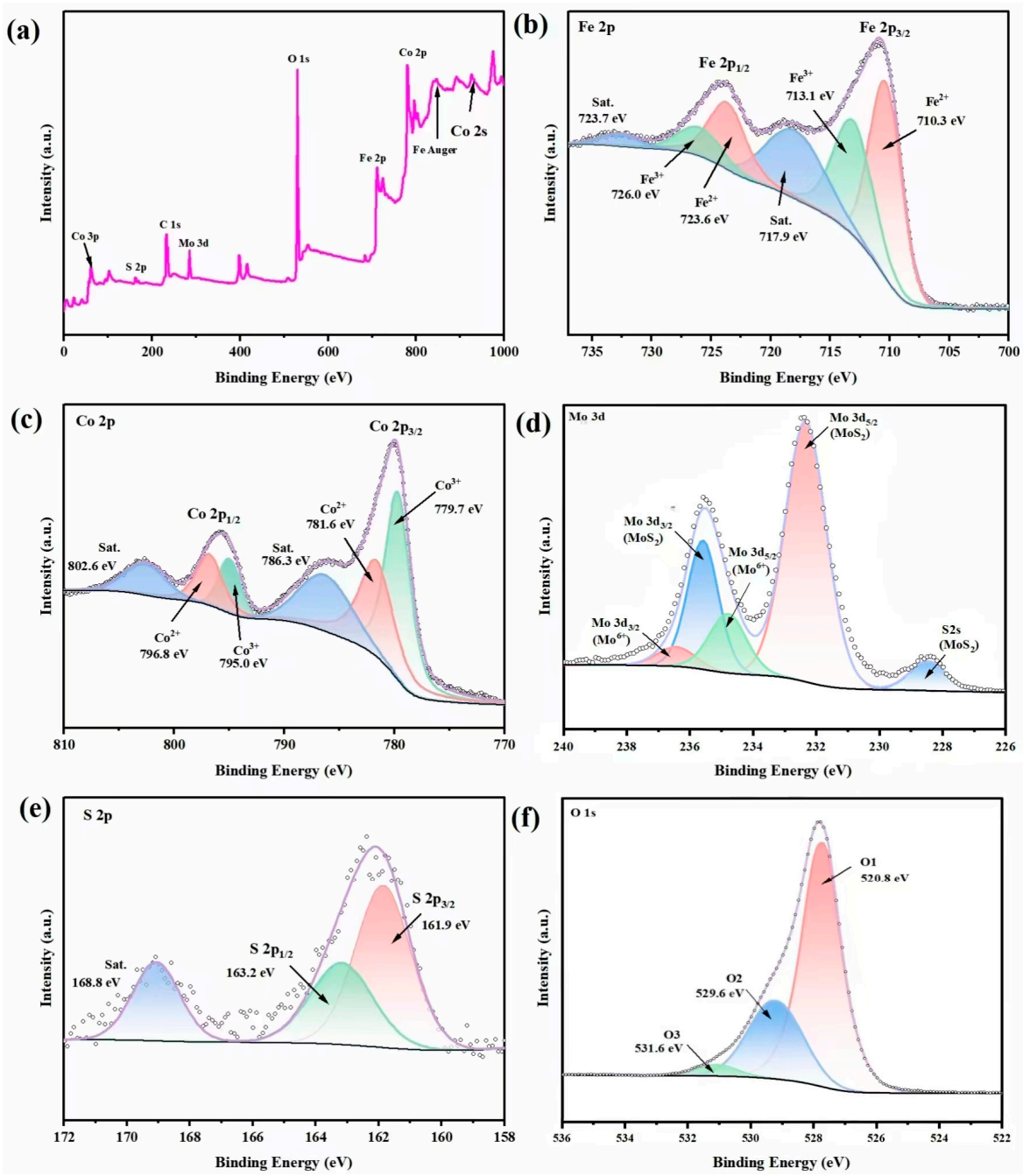

Figure 3. XPS spectra of FCO/MS-1: (**a**) full spectrum; (**b**) Fe 2p; (**c**) Co 2p; (**d**) Mo 3d; (**e**) S 2p; (**f**) O 1s.

Figure 3d shows the XPS spectrum of Mo 3d. The binding energies at 232.3 and 235.6 eV can be attributed to Mo(IV) $3d_{5/2}$ and Mo(IV) $3d_{3/2}$, respectively; the binding energies at 234.8 and 236.4 eV can be attributed to Mo(VI) $3d_{5/2}$ and Mo(VI) $3d_{3/2}$, respectively. In addition, the signal at 228.5 eV is attributed to the S 2s peak [34]. These results indicate that Mo predominantly exists in tetravalent and hexavalent forms in the composite catalysts.

Figure 3e shows the XPS spectrum of S 2p, with 161.9 and 163.2 eV corresponding to S $2p_{3/2}$ and S $2p_{1/2}$, respectively. These phenomenones may be related to S-Co bonding, and 168.8 eV can be attributed to the satellite peaks of the S [35].

Figure 3f shows the XPS spectrum of O 1s with the binding energies of 529.6, 520.8, and 531.6 eV corresponding to metal–oxygen bonds, surface oxygen ions, and surface physiosorbed water or chemisorbed water [36,37]. Combined with the previous characterization

results, this shows that the prepared composite catalysts are rich in redox electric pairs and illustrates the successful construction of a Co-S-Mo heterojunction. It facilitates rapid charge transfer, thereby increasing the conductivity and catalytic activity of the catalyst.

2.4. Electrochemical Properties of Catalysts

2.4.1. Hydrogen Evolution Performance

A three-electrode system with an electrolyte of 1 M KOH was used to conduct electrochemical tests on catalysts with different MoS_2 and doping ratios to explore the effects of MoS_2 and doping ratios on HER activity. The catalyst was activated at a scanning speed of 100 mV s^{-1} in a potential range of 0.2–0.4 V. After the activation completed, a linear sweep voltammetry test was performed at a scanning rate of 2 mV s^{-1}.

The test results shown in Figure 4a,c exhibit that MoS_2 had the most prominent hydrogen evolution activity, with overpotentials of 124 mV and 263 mV at current densities of 10 and 50 mA cm^{-2}, respectively. After adding MoS_2 to pure $FeCo_2O_4$, the composite catalyst FCO/MS-1 was prepared in 10 mA cm^{-2}. The overpotentials at the current density in 10 mA cm^{-2} were at 138 and 291 mV, which was significantly superior to the sample of FCO (234 and 358 mV), FCO/MS-2 (198 and 332 mV), and FCO/MS-3 (167 and 301 mV) samples. As the doping content of MoS_2 increases, the hydrogen evolution activity of the composite catalyst first increases. When the ratio of $FeCo_2O_4$ to MoS_2 is 1:1, the hydrogen evolution activity decreases. The composite catalyst FCO/MS-1 showed a 96 mV increase in hydrogen evolution activity compared to pure $FeCo_2O_4$. This result indicates that the cross-nanosheet structure of the catalyst and the heterojunction formed by doping with MoS_2 facilitated charge transfer, resulting in a decrease in hydrogen evolution overpotential.

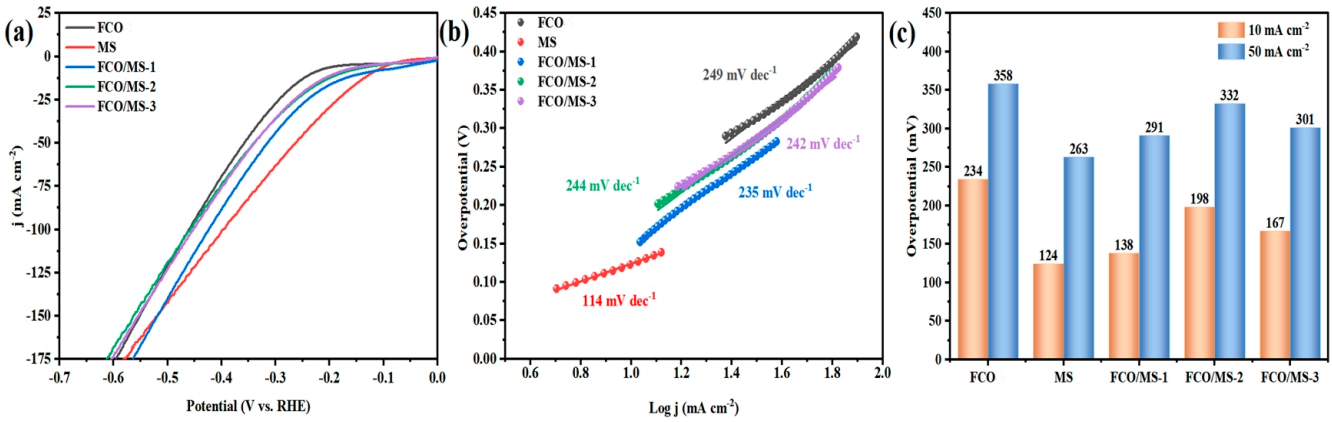

Figure 4. Catalytic performance of FCO, MS, FCO/MS-1, FCO/MS-2, and FCO/MS-3 catalysts: (**a**) polarization curves; (**b**) Tafel plots; (**c**) overpotentials at current densities of 10 and 50 mA cm^{-2}.

To study the reaction kinetics of the catalyst, the Tafel slope plot was obtained by fitting the polarization curve. The lower the Tafel value, the faster the current density of the potential increases [38]. As shown in Figure 4b, the Tafel slope of MoS_2 is 114 mV dec^{-1}, and the Tafel slope of the composite catalyst FCO/MS-1 is 235 mV dec^{-1}, which is lower compared to pure FCO (249 mV dec^{-1}), FCO/MS-2 (244 mV dec^{-1}), and FCO/MS-3 (242 mV dec^{-1}). The low Tafel value indicates that doped MoS_2 can change the electron valence state of the catalyst, effectively reduce the Tafel slope, and thus accelerate the catalyst hydrogen evolution reaction kinetics. In the alkaline electrolyte, due to the lack of H^+, H_2O replaces H^+ and then form adsorbed hydrogen (H*) with the coupled electron on the catalyst surface, and the cross-sheet structure of the composite catalyst provides more catalytic sites for electron transfer, resulting in a decrease in hydrogen evolution overpotential.

The area of electrochemical activity is an important index to evaluate the catalytic activity of catalysts. Using electrical double-layer capacitance (C_{dl}), we can calculate the electrochemical active area. To obtain the C_{dl} of the samples, the CV curves were tested at a

potential range of 0.2–0.3 V with the catalysts at different sweep velocities (20–100 mV s^{-1}), and the results are shown in Figure 5a–e. The set of curves of $FeCo_2O_4$ is shown as a regular rectangle, which indicates that $FeCo_2O_4$ has good capacitance characteristics. The set of curves of MoS_2 is shown as a class rectangle, and the set of the composite catalyst $FeCo_2O_4/MoS_2$ prepared by introducing MoS_2 appears the same. By performing a linear fit on the difference in current density (Δj/2) and the scanning rate, we can obtain the double-layer capacitance value of the catalyst.

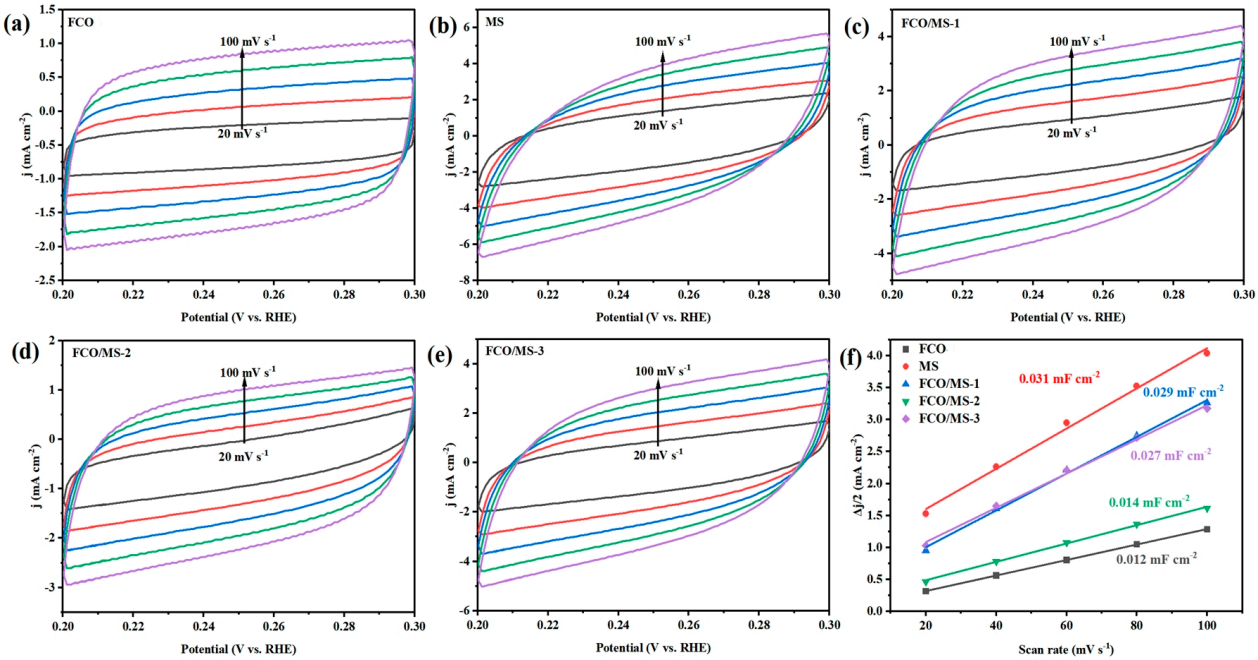

Figure 5. Cyclic voltammograms of HER in the non-Faradaic potential range (0.2–0.3 V) at different scan rates (20, 40, 60, 80 and 100 mV s^{-1}) in different colors: (**a**) FCO; (**b**) MS; (**c**) FCO/MS-1; (**d**) FCO/MS-2; (**e**) FCO/MS-3; (**f**) double-layer capacitance of the catalysts for HER.

The C_{dl} of the catalyst is shown in Figure 5f; the C_{dl} value of MoS_2 is 0.031 mF cm^{-2}, that of $FeCo_2O_4$ is 0.012 mF cm^{-2}, and that of FCO/MS-2 is 0.014 mF cm^{-2}. The C_{dl} value of FCO/MS-3 is 0.027 mF cm^{-2}, while the C_{dl} value of FCO/MS-1 is 0.029 mF cm^{-2}. And the C_{dl} of the synthesized composite catalyst FCO/MS-1 is twice that of the pure $FeCo_2O_4$.

The electrochemical surface area (*ECSA*) values can be calculated according to the double-layer capacitance, and *ECSA* can reflect the number of active sites of the catalyst to a certain extent. The calculation formula is as follows, where C_s is the capacitance per unit area of the smooth plate surface of the material, and C_s in an alkaline solution is 40 μF cm^{-2} [39].

$$ECSA = \frac{C_{dl}}{C_s} \quad (1)$$

According to Equation (1), the *ECSA* value of the catalyst can be calculated. The *ECSA* value of MoS_2 is 0.775 and the *ECSA* value of $FeCo_2O_4$ is 0.3, while the *ECSA* value of FCO/MS-2 is 0.35, the *ECSA* value of FCO/MS-3 is 0.675, and the *ECSA* value of FCO/MS-1 is 0.725. This indicates that the introduction of MoS_2 enlarges the electrochemical active area of the composite catalyst $FeCo_2O_4/MoS_2$ and increases the catalytic active site of the catalyst, which can effectively improve HER catalytic activity.

Furthermore, in order to further study the reaction kinetics of the catalyst, all the impedance spectroscopy of the catalyst in the range of 0.1–1 MHz was tested, while the equivalent circuit was fitted using Zview software(2.0.0.10). The equivalent circuit diagram of the catalyst can be simplified as the illustration in Figure 6, which combines it with the solution resistance (R_s), interface resistance (R_{sp}), charge transfer resistance (R_{ct}), and

constant phase angle element (CPE). In the Nyquist plot, the left side is the high-frequency and the right side is the low-frequency region. The first semicircle diameter in the high-frequency region can be expressed as the interface resistance, which is caused by the electrochemical reaction happening on the contact surface between the electrode and the electrolyte. The semicircle diameter appearing in the low-frequency range can be expressed as the charge transfer resistance of the catalyst. Usually, a small value of charge transfer resistance means faster reaction kinetics; the higher the charge transfer rate means the better catalytic activity.

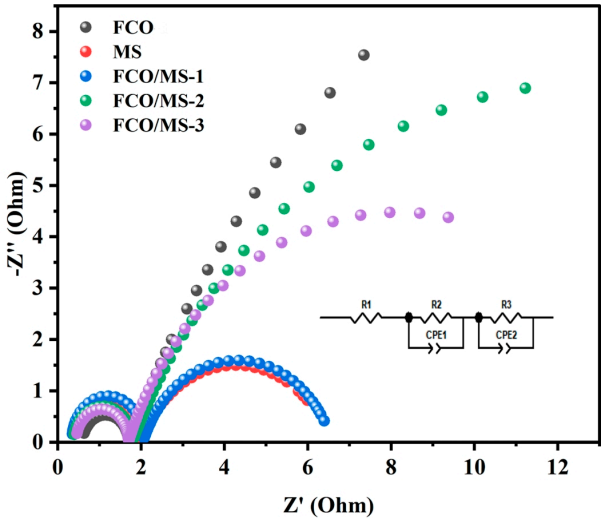

Figure 6. Nyquist plots of FCO, MS, FCO/MS-1, FCO/MS-2, and FCO/MS-3 catalysts at a current density of 10 mA cm^{-2}, with the inset showing the corresponding equivalent circuit diagram.

Table 1 shows the fitting circuit diagram data of the AC impedance test of the catalyst, which indicate that the charge transfer resistance of the composite catalyst $FeCo_2O_4/MoS_2$ is 4.6 Ω, the charge transfer resistance of MoS_2 is 4.6 Ω, and the charge transfer resistance of $FeCo_2O_4$ is 40 Ω. The results above indicate that the heterojunction structure formed by the composite catalyst $FeCo_2O_4/MoS_2$ doped with MoS_2 can accelerate the charge transfer rate, reduce the charge transfer resistance, and finally improve the hydrogen evolution performance of the catalyst.

Table 1. AC impedance test fitting circuit data for catalysts.

Sample	Element	Resistance Value (Ω)	Error	Error %
FCO	R_s	0.59	0.014	2.4
	R_{sp}	1.1	0.018	1.7
	R_{ct}	40	5.6	9.8
MS	R_s	0.39	0.010	2.6
	R_{sp}	1.6	0.020	1.2
	R_{ct}	4.6	0.16	3.6
FCO/MS-1	R_s	0.34	0.0087	2.5
	R_{sp}	1.7	0.019	1.1
	R_{ct}	4.6	0.13	2.9
FCO/MS-2	R_s	0.37	0.011	3.0
	R_{sp}	1.4	0.019	1.4
	R_{ct}	22	1.5	6.8
FCO/MS-3	R_s	0.44	0.010	2.4
	R_{sp}	1.3	0.015	1.2
	R_{ct}	13	0.50	3.8

Stability is also an important parameter to measure catalysts in practical applications. Therefore, the stability of FCO/MS-1 was tested using chronopotentiometry. The change in catalyst potential was observed at a fixed current density. As shown in Figure 7, the overpotential of FCO/MS-1 did not change significantly, indicating that the FCO/MS-1 sample had good catalytic stability and had almost no change in potential after continuous operation at a current density of 10 mA cm^{-2} for 10 h.

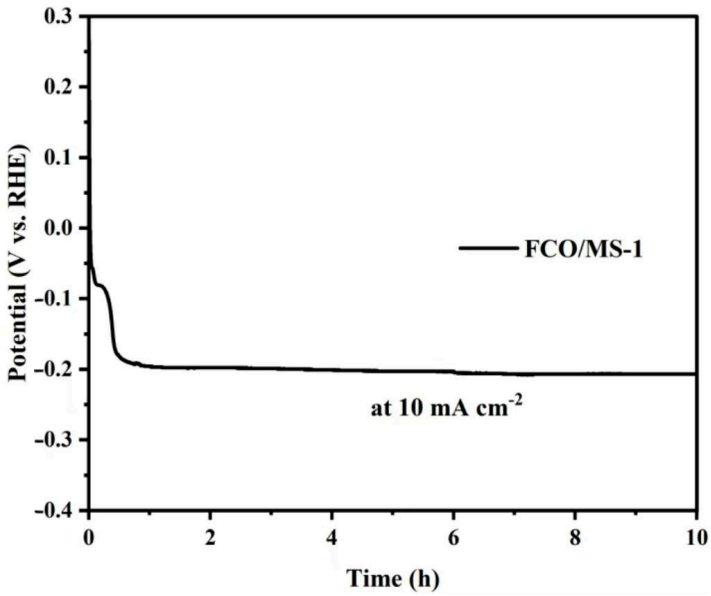

Figure 7. Chronopotentiometry curve of FCO/MS-1 catalyst about hydrogen evolution performance at a current density of 10 mA cm^{-2}.

2.4.2. Oxygen Evolution Performance

The composite catalyst $FeCo_2O_4/MoS_2$ not only has better HER performance, but also has better OER performance. The catalyst was activated at a scanning speed of 100 mV s^{-1} in the potential range of 1.05–1.35 V. After the activation was completed, the linear scanning voltammetry test was performed, and the scanning rate was 2 mV s^{-1}. Due to the strong oxidation peak of the catalyst during forward LSV scanning, it was difficult to determine the corresponding overpotential at a low current density. Therefore, we used reverse scanning to convert the oxidation peak to the reduction peak to avoid the influence of the oxidation peak on the overpotential at a low current density.

The results in Figure 8a,c show that the composite catalyst $FeCo_2O_4/MoS_2$ has better OER activity. The overpotentials are 244 and 333 mV at 10 and 50 mA cm^{-2} current densities, below the FCO (282 and 399 mV), FCO/MS-3 (235 and 343 mV), FCO/MS-2 (269 and 369 mV), and MS (367 and 535 mV) samples. This indicates that the composite catalyst constructed by doping MoS_2 in pure $FeCo_2O_4$ has an improved oxygen precipitation performance compared to pure $FeCo_2O_4$, with the overpotential reduced by 38 mV. The oxygen evolution overpotential of FCO/MS-3 was also enhanced compared to pure $FeCo_2O_4$, with an overpotential reduction of 47 mV, but the combined HER was greater for the FCO/MS-1 catalyst in terms of the simultaneous enhancement of both OER and HER activities, and thus this paper focuses on illustrating the FCO/MS-1 catalyst.

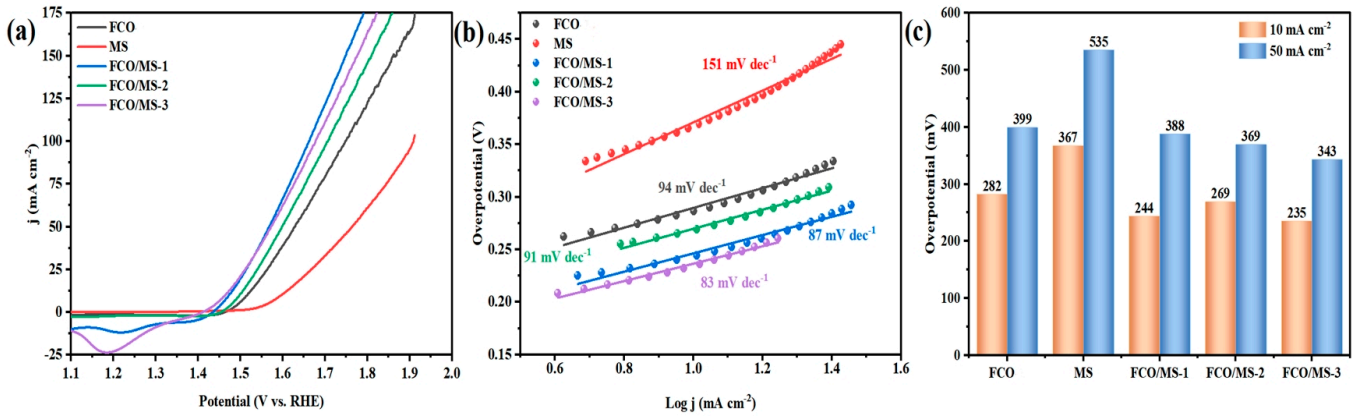

Figure 8. Catalytic performance of catalysts FCO, MS, FCO/MS-1, FCO/MS-2, and FCO/MS-3: (**a**) polarization curves; (**b**) Tafel plots; (**c**) overpotentials at 10 and 50 mA cm^{-2} current densities.

Figure 8b shows Tafel slope plots for MS (151 mV dec^{-1}), FCO (94 mV dec^{-1}), and FCO/MS-2 (91 mV dec^{-1}), and FCO/MS-3 exhibited Tafel slopes as low as 83 mV dec^{-1}, indicating rapid OER catalytic kinetics. The low Tafel slope of the composite catalyst FCO/MS-1 (87 mV dec^{-1}) compared to pure $FeCo_2O_4$ also indicates its faster OER catalytic kinetics. The excellent catalytic activity and fast reaction kinetics of the composite catalysts result from the synergistic effect between the catalyst components. During the OER process, the abundant redox electric pairs (Co^{2+}/Co^{3+}, Fe^{2+}/Fe^{3+}) adsorbed OH^- and improved the OER activity. The coexistence of Co^{2+}/Co^{3+}, Fe^{2+}/Fe^{3+}, and in the catalyst can be confirmed from the XPS analysis in Figure 3. The above results indicate that more catalytic sites were exposed on the surface of the composite catalyst FCO/MS-1 by constructing the cross-nanosheet structure of the catalyst, which accelerated the charge transfer for more efficient mass transfer.

Similarly, we studied the C_{dl} capacitance of the oxygen evolution reaction (OER). Figure 9a–e show the cyclic voltammetry curves obtained at different scan rates (2–12 mV s^{-1}) in the non-Faradaic region (1.05–1.15 V vs. RHE). The catalyst exhibits a quasi-rectangular shape in the CV curves, indicating its capacitance characteristics. The double-layer capacitance of the catalyst is determined by linear fitting of the current density difference ($\Delta j/2$) from the CV curves against the scan rate. Figure 9f shows the C_{dl} of the catalyst, where the C_{dl} value is 0.010 mF cm^{-2} for MS, 0.058 mF cm^{-2} for FCO, 0.37 mF cm^{-2} for FCO/MS-2, and 0.52 mF cm^{-2} for FCO/MS-3; the C_{dl} of FCO/MS-1 is 0.41 mF cm^{-2}. Compared with pure $FeCo_2O_4$, the C_{dl} of FCO/MS-1 increased by seven times. The electrochemical surface area (*ECSA*) values were calculated based on the double-layer capacitance, resulting in *ECSA* values of 0.25 for MS, 1.45 for FCO, 9.25 for FCO/MS-2, 13 for FCO/MS-3, and 10.45 for FCO/MS-1 according to Equation (1). This indicates a significant enhancement in the electrochemical surface area of the catalyst by doping MoS_2 into pure $FeCo_2O_4$, increasing the active sites for the OER performance of the catalyst.

Similar to HER, electrochemical impedance tests were conducted on all catalysts, and equivalent circuit fitting was performed using Zview software. The equivalent circuit diagram of the catalyst can be simplified as in the illustration in Figure 10, consisting of solution resistance (R_s), interface resistance (R_{sp}), charge transfer resistance (R_{ct}), and the constant phase angle element (CPE). Nyquist is composed of two semicircles, with the semicircle in the high-frequency region being the interface resistance and the second semicircle in the low-frequency region being the charge transfer resistance. In the Nyquist plot, a smaller semicircle indicates that the catalyst has a smaller charge transfer resistance and fast charge transfer rate.

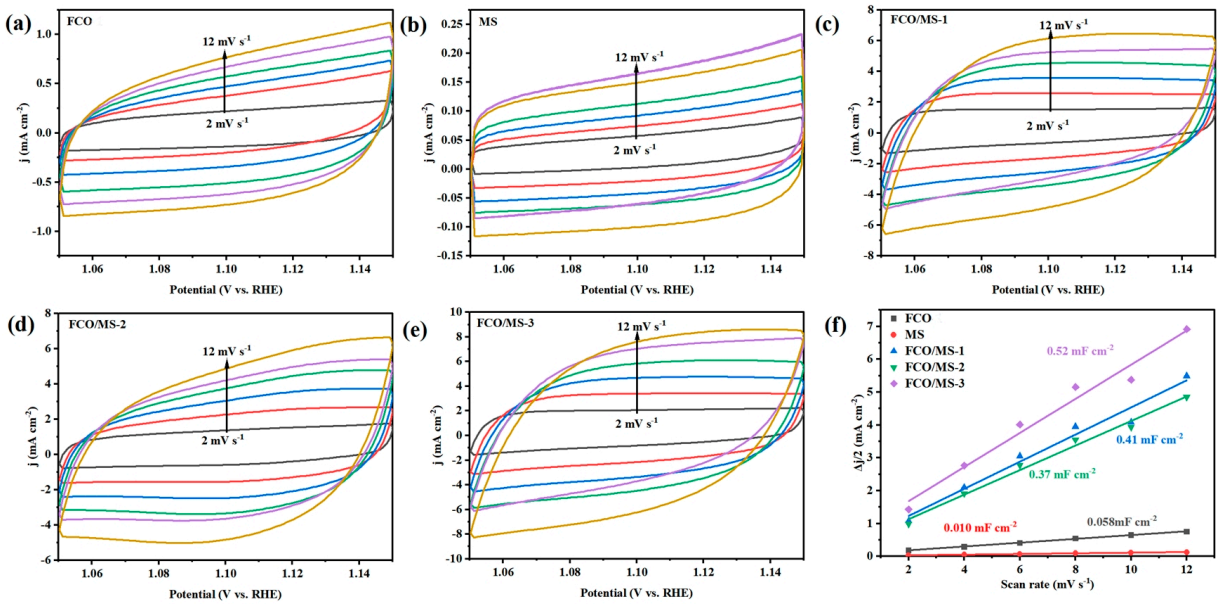

Figure 9. Cyclic voltammograms of OER in the non-Faradaic potential range (1.05–1.15 V vs. RHE) at different scan rates (2, 4, 6, 8, 10 and 12 mV s^{-1}) in different colors: (**a**) FCO; (**b**) MS; (**c**) FCO/MS-1; (**d**) FCO/MS-2; (**e**) FCO/MS-3; (**f**) double-layer capacitance of the catalysts for OER.

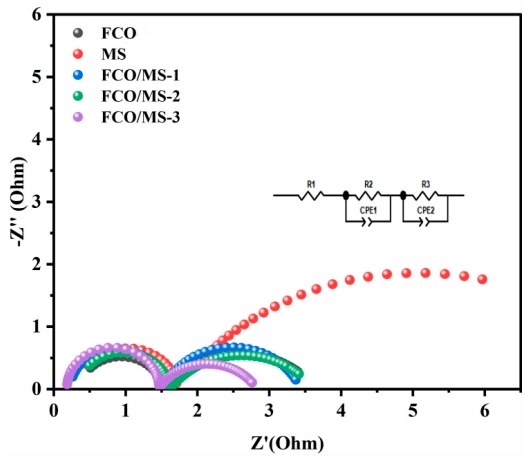

Figure 10. Nyquist plots of catalysts FCO, MS, FCO/MS-1, FCO/MS-2, and FCO/MS-3 at a current density of 10 mA cm^{-2}, with the inset showing the corresponding equivalent circuit diagram.

Table 2 shows the fitted circuit diagram data for catalyst AC impedance testing. The charge transfer resistance of sample FCO/MS-1 is 1.4 Ω, the charge transfer resistance of FCO/MS-3 is 1.3 Ω, the charge transfer resistance of FCO/MS-2 is 2.0 Ω, the charge transfer resistance of MS is 6.7 Ω, and the charge transfer resistance of FCO is 2.1 Ω. After the introduction of MoS_2, the charge transfer resistance of the $FeCo_2O_4/MoS_2$ composite catalyst decreased. This result indicates that the heterojunction structure constructed by $FeCo_2O_4$ and MoS_2 can promote the electron transfer process, increase the conductivity of the catalyst, and enhance the catalytic activity of the catalyst.

In practical applications, stability is also an important parameter. Therefore, a chronopotentiometry test of the composite catalyst FCO/MS-1 was carried out at a current density of 10 mA cm^{-2} to measure the stability of the catalyst. The results are shown in Figure 11. In the 1 M KOH electrolyte, the voltage of FCO/MS-1 remained unchanged after running for 10 h at a current density of 10 mA cm^{-2}, indicating that the FCO/MS-1 sample had good catalytic stability.

Table 2. Fitted circuit data from AC impedance tests of catalysts.

Sample	Element	Resistance Value (Ω)	Error	Error %
FCO	R_s	0.35	0.016	4.6
	R_{sp}	1.2	0.019	1.6
	R_{ct}	2.1	0.051	2.4
MS	R_s	0.33	0.031	9.4
	R_{sp}	1.4	0.047	3.4
	R_{ct}	6.7	0.47	7.0
FCO/MS-1	R_s	0.18	0.0041	2.2
	R_{sp}	1.3	0.012	1.0
	R_{ct}	1.4	0.051	3.7
FCO/MS-2	R_s	0.33	0.016	4.8
	R_{sp}	1.3	0.019	1.5
	R_{ct}	2.0	0.049	2.4
FCO/MS-3	R_s	0.23	0.0064	2.8
	R_{sp}	1.9	0.036	1.9
	R_{ct}	1.3	0.0099	0.76

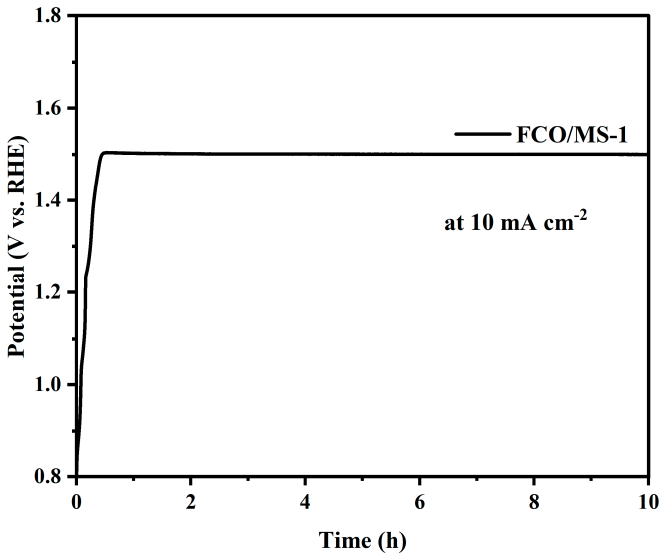

Figure 11. Chronopotentiometry curve of FCO/MS-1 catalyst about oxygen evolution performance at a current density of 10 mA cm^{-2}.

2.4.3. Performance of $FeCo_2O_4/MoS_2$ Catalyst under Overall Water Splitting

The electrochemical test results mentioned above indicate that the composite catalyst $FeCo_2O_4/MoS_2$ exhibits excellent catalytic activity in both the OER and HER processes. Assembled as an anode and cathode, respectively, the $FeCo_2O_4/MoS_2$ two-electrode system was tested for overall water splitting performance in a 1 M KOH electrolyte with a scan rate of 2 mV s^{-1}.

The test results, as shown in Figure 12a, reveal that the water decomposition voltage of $FeCo_2O_4/MoS_2$ at a current density of 10 mA cm^{-2} is 1.59 V, indicating its favorable overall water splitting performance. Additionally, the composite catalyst $FeCo_2O_4/MoS_2$ exhibits good stability under alkaline conditions, as demonstrated by chronoamperometry testing, with a current retention rate of 98.5% after continuous operation for 10 h, as shown in Figure 12b. The discussed results suggest that $FeCo_2O_4/MoS_2$ possesses both excellent catalytic activity and stability in the OER and HER processes.

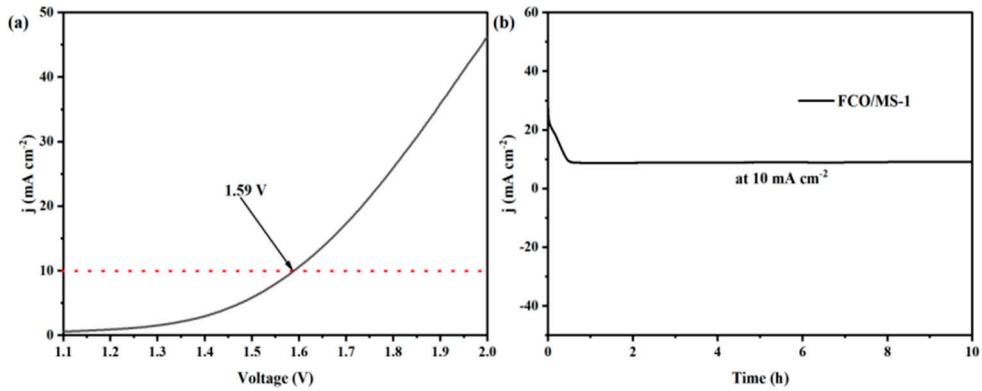

Figure 12. Water electrolysis performance of FCO/MS-1 catalyst (The red dashed line represents j = 10mA cm^{-2}): (**a**) LSV polarization curves for water electrolysis; (**b**) chronoamperometric curve at a constant voltage of 1.59 V for the water electrolysis test.

The $FeCo_2O_4/MoS_2$ two-electrode system was tested for overall water splitting performance in a 1 M KOH electrolyte with a scan rate of 2 mV s^{-1}. Figure 13 illustrates recent electrocatalysts used for water electrolysis to produce hydrogen. Material proof shows that using a rechargeable Zn-air battery with the Co@N-CNTF as an ORR/OER bifunctional catalyst on air electrodes, can operate under ambient conditions with high cycling stability. As a proof of concept, the Co@N-CNTF as an OER/HER bifunctional catalyst for full water splitting affords an alkaline condition with 10 mA cm^{-2} under a stable voltage of 1.71 V [13].

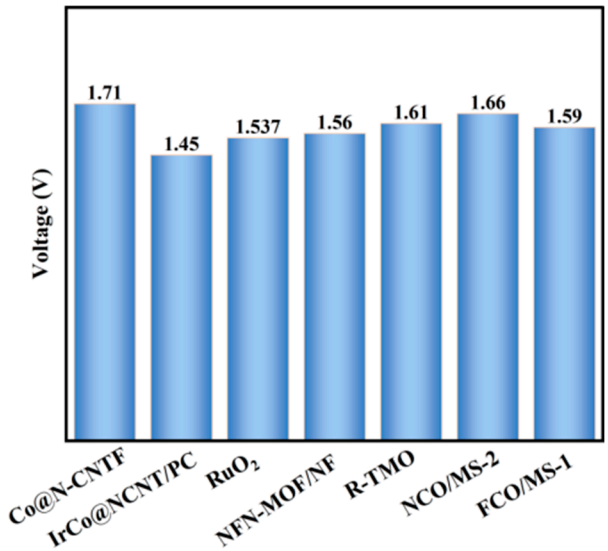

Figure 13. Water electrolysis catalysts.

While low-loading iridium (Ir) (≈2.3 wt%)-decorated cobalt nanoparticles are embedded in nitrogen-doped carbon nanotube/porous carbon sheets (IrCo@NCNT/PC), then prepared to serve as the OER/HER/ORR trifunctional electrocatalyst, a low cell voltage of 1.45 V is required at j = 10 mA cm^{-2} (j_{10}) for overall water splitting (OWS) in the alkaline electrolytes. And when $MoS_2/NiCo_2O_4$/NF was at 10 mA cm^{-2}, NCO/MS-2 achieved a quite low voltage of 1.62 V and exhibited satisfactory stability for 16 h [40].

As can be seen from the diagram, the voltage of the water was reduced to 1.45 V. The prepared composite catalyst $FeCo_2O_4/MoS_2$ exhibits comparable activity to some previously reported catalysts, such as R-TMO, NFN-MOF/NF, and Co@N-CNTF.

3. Experimental Section

3.1. Materials

The concentrated cobalt chloride hexahydrate ($CoCl_2 \cdot 6H_2O \geq 99\%$), concentrated ferric chloride hexahydrate ($FeCl_3 \cdot 6H_2O \geq 99\%$), concentrated sodium molybdate dihydrate ($Na_2MoO_4 \cdot 2H_2O \geq 99\%$), concentrated urea ($(NH_2)_2CO \geq 98\%$), and potassium hydroxide ($KOH \geq 85\%$) were from Shanghai Aladdin Bio Chem Technology Co., Ltd. (Shanghai, China). The concentrated thioacetamide ($C_2H_5NS \geq 99\%$), concentrated ammonium fluoride ($NH_4F \geq 96\%$), hydrochloric acid (HCl), conductive Ketien carbon black (Nanjing, China), and polyvinylidene fluoride (PVDF) were from Sinopharm Chemical Reagent Co. (Shanghai, China).

3.2. Preparation Process

3.2.1. Preparation of $FeCo_2O_4$

$FeCo_2O_4$ was prepared by a combination of a hydrothermal method and calcination. Firstly, hexahydrate iron chloride ($FeCl_3 \cdot 6H_2O$) and hexahydrate cobalt chloride ($CoCl_2 \cdot 6H_2O$) were added in a molar ratio of 1:2 to 60 mL of deionized water, and stirred until completely dissolved. Then, urea ($(NH_2)_2CO$) and ammonium fluoride (NH_4F) were added in a molar ratio of 5:3 to the mixed solution and stirred until completely dissolved. Finally, the mixed solution was transferred to a stainless-steel high-pressure reactor lined with polytetrafluoroethylene (PTFE) (100 mL) and placed in an oven at 120 °C for 10 h of reaction. After the reaction was completed, the obtained solution was centrifuged, washed several times alternately with deionized water and ethanol, and dried overnight at 70 °C in an oven. Finally, the obtained solid powder was calcined at 350 °C for 2 h at a heating rate of 10 °C/min in a muffle furnace to obtain the final product $FeCo_2O_4$.

3.2.2. Preparation of MoS_2

Firstly, sodium molybdate dihydrate ($Na_2MoO_4 \cdot 2H_2O$) and thioacetamide (C_2H_5NS) were added in a molar ratio of 1:3.5 to 60 mL of deionized water, then stirred it until the mixed solution was homogeneous and dispersed formed. Then, the mixed solution was transferred to a stainless-steel high-pressure reactor (100 mL) lined with PTFE, the reactor was placed in an oven reacting at 200 °C for 15 h. After the reaction was completed, the obtained solution was centrifuged, and it was washed several times with deionized water and ethanol. Finally, it was dried overnight at 70 °C, and the obtained solid was ground into powder to obtain MoS_2.

3.2.3. Preparation of $FeCo_2O_4/MoS_2$

Firstly, the synthesized $FeCo_2O_4$ was uniformly dispersed in 30 mL deionized water to form a mixed liquor. Secondly, $Na_2MoO_4 \cdot 2H_2O$ and C_2H_5NS were added to the mixed liquor in a molar ratio of 1:3.5. Thirdly, the mixed liquor was transferred to a stainless-steel autoclave (100 mL) lined with PTFE. The autoclave was placed in an oven and reacted at 200 °C for 15 h. After the reaction was completed, the obtained liquor was centrifuged, and it was washed several times with deionized water and ethyl alcohol. Finally, it was dried in an oven at 70 °C overnight, and the obtained solid was ground into powder to obtain $FeCo_2O_4/MoS_2$. The preparation process diagram of $FeCo_2O_4/MoS_2$ is shown in Scheme 1. Three separate composite catalysts of 1:0.3, 1:0.7, and 1:1 were prepared by adding different-quality molybdenum sources. The specific preparation parameters and sample numbers of $FeCo_2O_4/MoS_2$ are shown in Table 3. FCO/MS-1 means the composition is 1:0.3, FCO/MS-2 means the composition is 1:0.7, and FCO/MS-3 means the composition is 1:1.

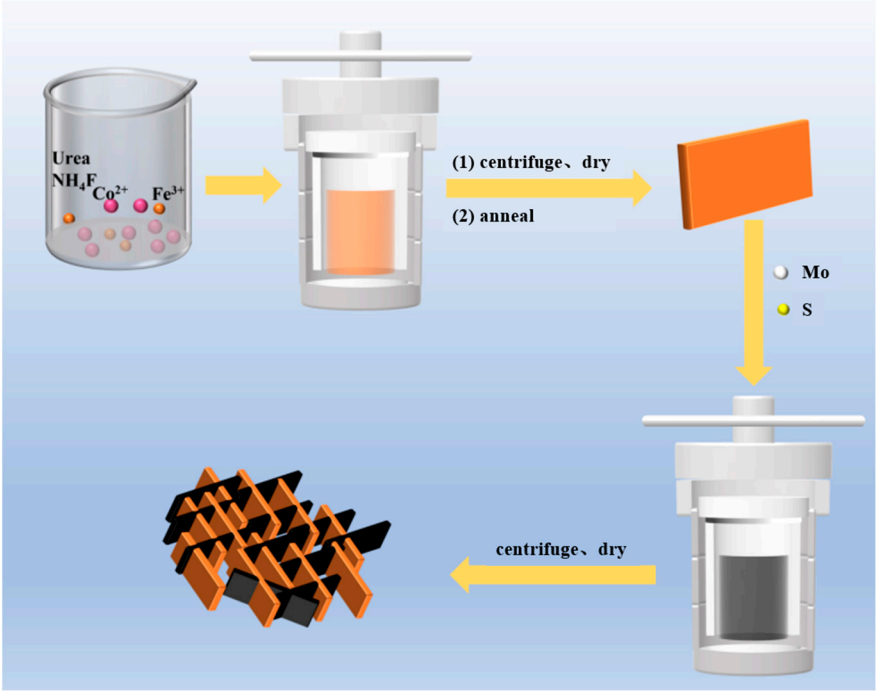

Scheme 1. Preparation process of $FeCo_2O_4/MoS_2$ composite catalysts.

Table 3. Preparation parameters for $FeCo_2O_4/MoS_2$ catalysts.

Catalyst Name	Sample Number	Hydrothermal Temperature (°C)	Composite Ratio
$FeCo_2O_4/MoS_2$	FCO/MS-1	120 °C, 10 h/200 °C, 15 h	1:0.3
	FCO/MS-2		1:0.7
	FCO/MS-3		1:1

3.3. Characterization

The scanning electron microscope (SEM, JSM-7610FPlus, JEOL, Tokyo, Japan) is an instrument that uses a focused high-energy electron beam to scan the surface of a material and stimulate a variety of physical information. By receiving, amplifying, and displaying this physical information, the surface morphology of the sample is gained. At the same time, energy dispersive X-ray spectroscopy (EDS) characterization was performed using an energy dispersive spectrometer loaded on a scanning electron microscope to determine the type, composition, and content of the elements contained in the sample for quantitative analysis.

X-ray diffraction (XRD, D8 Advance, Bruker AXS, Karlsruhe, Germany) is a method to analyze and determine the existence form of each component in the sample. It is based on the diffraction effect of polycrystalline samples on X-rays. The crystal structure and phase composition of the material can be determined by comparing the XRD patterns with the standard card. During the test, an appropriate amount of the powder sample was tiled in the sample tank of the glass slide. The type of radiation was Cu-Kα, the voltage was set at 40 kV, the current was 200 mA, the scanning range was 5–80°, and the scanning speed was 5° min^{-1}.

X-ray photoelectron spectroscopy (XPS, ESCALAB 250 Xi, Thermo Fisher, Waltham, MA, USA) is a surface analysis technique that uses X-rays to radiate the surface of a sample to excite photoelectrons, and determines the type, content, and valence state of the elements by measuring the kinetic energy of the photoelectrons.

3.4. Electrochemical Performance Test

All the electrochemical tests were performed at the CHI760E electrochemical workstation. The electrolyte was 1 M KOH (pH = 13.8). The standard three-electrode system

was used to test OER and HER performance, and the two-electrode system was used for the total water splitting test. The working electrode was a self-supporting electrode (1×1 cm^2), the graphite sheet was used as the counter electrode, and Hg/HgO was the reference electrode.

$$E(RHE) = E(vs.\ Hg/HgO) + 0.059 \times pH + 0.098\ V$$

Preparation method for the self-supporting electrode: Weighed the prepared powder sample, polyvinylidene fluoride (PVDF), and conductive carbon black (at the mass ratio of 8:1:1) and placed them in a mortar, and then added a certain amount of methylmercuric iodide pyrrolidone (NMP). Fully grind them to form slurry, then evenly coat the obtained slurry on foam nickel(NF) and dry them in the oven at 60 °C for a while.

4. Conclusions

An $FeCo_2O_4/MoS_2$ composite was prepared by the hydrothermal method and calcination method, and then the $FeCo_2O_4/MoS_2$ composite was synthesized under certain conditions. The performance of the composite catalyst was affected by the molybdenum source. The electrochemical test results show that the composite catalyst has good OER and HER catalytic activity when the ratio of $FeCo_2O_4$ to MoS_2 is 1:0.3. At a current density of 10 mA cm^{-2}, the hydrogen evolution overpotential is 138 mV and the oxygen evolution overpotential is 244 mV, while pure $FeCo_2O_4$ has a hydrogen evolution overpotential of 234 mV and an oxygen evolution overpotential of 282 mV. The hydrogen evolution and oxygen evolution performance were improved by 96 mV and 38 mV, respectively. The alkaline electrolysis cell was assembled using $FeCo_2O_4/MoS_2$ as the cathode and anode, respectively. In a 1 M KOH electrolyte, the voltage of fully hydrolyzed water at a current density of 10 mA cm^{-2} was 1.59 V, and it maintained good stability in a 10 h electrolysis water test, with a current retention rate of 98.5%.

Author Contributions: Conceptualization, M.Z.; Software, Z.L.; Formal analysis, Y.W.; Investigation, S.Z.; Data curation, Z.L.; Writing—original draft, Z.C.; Writing—review & editing, Z.C.; Supervision, Y.C.; Funding acquisition, Y.C. All authors have read and agreed to the published version of the manuscript.

Funding: This reaserch was funded by the "College Students' Innovation and Entrepreneurship Training Program" (No. 2024-628).

Data Availability Statement: Data are contained within the article.

Acknowledgments: The authors are thankful for the facilities provided by the instruments and equipment-sharing platform of the China University of Geosciences (Beijing).

Conflicts of Interest: The authors declare no conflict of interest.

References

1. Huang, J.; Jiang, Y.; An, T.; Cao, M. Increasing the active sites and intrinsic activity of transition metal chalcogenide electrocatalysts for enhanced water splitting. *J. Mater. Chem. A* **2020**, *8*, 25465–25498. [CrossRef]
2. Wang, S.; Lu, A.; Zhong, C.J. Hydrogen production from water electrolysis: Role of catalysts. *Nano Converg.* **2021**, *8*, 4–27. [CrossRef]
3. Turner, J.A. Sustainable Hydrogen Production. *Science* **2004**, *305*, 972–974. [CrossRef]
4. Niksa, S. FLASHCHAIN Theory for Rapid Coal Devolatilization Kinetics. 10. Extents of Conversion for Hydropyrolysis and Hydrogasification of Any Coal. *Energy Fuels* **2018**, *32*, 384–395. [CrossRef]
5. Muradov, N. Hydrogen via methane decomposition: An application for decarbonization of fossil fuels. *Int. J. Hydrogen Energy* **2001**, *26*, 1165–1175. [CrossRef]
6. Abdelhamid, H.N. A review on hydrogen generation from the hydrolysis of sodium borohydride. *Int. J. Hydrogen Energy* **2021**, *46*, 726–765. [CrossRef]
7. Torres-Pinto, A.; Sampaio, M.J.; Silva, C.G.; Faria, J.L. Recent Strategies for Hydrogen Peroxide Production by Metal-Free Carbon Nitride Photocatalysts. *Catalysts* **2019**, *9*, 990. [CrossRef]
8. Zhang, J.; Zhang, Q.; Feng, X. Support and interface effects in water-splitting electrocatalysts. *Adv. Mater.* **2019**, *31*, 8167–8186. [CrossRef]

9. Shang, X.; Liu, Z.Z.; Lu, S.S.; Dong, B.; Chi, J.Q.; Qin, J.F.; Liu, X.; Chai, Y.M.; Liu, C.G. Pt-C interfaces based on electronegativity-functionalized hollow carbon spheres for highly efficient hydrogen evolution. *ACS Appl. Mater. Interfaces* **2018**, *10*, 43561. [CrossRef]
10. Cherevko, S.; Geiger, S.; Kasian, O.; Kuiyk, N.; Grote, J.; Savan, A.; Shrestha, B.R.; Merzlikin, S.; Breitbach, B.; Ludwig, A.; et al. Oxygen and hydrogen evolution reactions on Ru, RuO_2, Ir, and IrO_2 thin film electrodes in acidic and alkaline electrolytes: A comparative study on activity and stability. *Catal. Today* **2016**, *262*, 170–180. [CrossRef]
11. Tang, S.; Zhou, X.; Liu, T.; Zhang, S.; Yang, T.; Luo, Y.; Sharman, E.; Jiang, J. Single nickel atom supported on hybridized graphene-boronnitride nanosheet as a highly active bi-functional electrocatalyst for hydrogen and oxygen evolution reactions. *J. Mater. Chem. A* **2019**, *7*, 26261–26265. [CrossRef]
12. Bu, Y.; Jang, H.; Gwon, O.; Kim, S.; Joo, S.; Nam, G.; Kim, S.; Qin, Y.; Zhong, Q.; Kwak, S. Synergistic interaction of perovskite oxides and N-doped graphene in versatile electrocatalyst. *J. Mater. Chem. A* **2019**, *7*, 2048–2054. [CrossRef]
13. Guo, H.; Feng, Q.; Zhu, J.; Xu, J.; Li, Q.; Liu, S.; Xu, K.; Zhang, C.; Liu, T. Cobalt nanoparticle-embedded nitrogen-doped carbon/carbon nanotube frameworks derived from a metal-organic framework for tri-functional ORR, OER and HER electrocatalysis. *J. Mater. Chem. A* **2019**, *7*, 3664–3672. [CrossRef]
14. Yu, H.; Xue, Y.; Hui, L.; He, F.; Zhang, C.; Liu, Y.; Fang, Y.; Xing, C.; Li, Y.; Liu, H.; et al. Graphdiyne-engineered heterostructures for efficient overall water-splitting. *Nano Energy* **2019**, *64*, 103928. [CrossRef]
15. Gao, J.; Li, Y.; Yu, X.; Ma, Y. Graphdiyne reinforced multifunctional Cu/Ni bimetallic Phosphides-Graphdiyne hybrid nanostructure as high performance electrocatalyst for water splitting. *J. Colloid Interface Sci.* **2022**, *628*, 508–518. [CrossRef]
16. Cao, C.; Ma, D.D.; Xu, Q.; Wu, X.T.; Zhu, Q.L. Semisacrificial template growth of self-supporting MOF nanocomposite electrode for efficient electrocatalytic water oxidation. *Adv. Funct. Mater.* **2018**, *29*, 1807418. [CrossRef]
17. Zhang, K.; Zou, R. Advanced transition metal-based OER electrocatalysts: Current status, opportunities, and challenges. *Small* **2021**, *17*, 2100129. [CrossRef]
18. Muthurasu, A.; Maruthapandian, V.; Kim, H.Y. Metal-organic framework derived Co_3O_4/MoS_2 heterostructure for efficient bifunctional electrocatalysts for oxygen evolution reaction and hydrogen evolution reaction. *Appl. Catal. B Environ.* **2019**, *248*, 202–210. [CrossRef]
19. Tyndall, D.; Gannon, L.; Hughes, L.; Carolan, J.; Pinilla, S.; Jaśkaniec, S.; Spurling, D.; Ronan, O.; McGuinness, C.; McEvoy, N.; et al. Understanding the effect of MXene in a TMO/MXene hybrid catalyst for the oxygen evolution reaction. *npj 2D Mater. Appl.* **2023**, *7*, 15. [CrossRef]
20. Liu, Q.; Huang, J.; Zhao, Y.; Cao, L.; Li, K.; Zhang, N.; Yang, D.; Feng, L.; Feng, L. Tuning the coupling interface of ultrathin $NisS_2$@NiV-LDH heterogeneous nanosheet electrocatalysts for improved overall water splitting. *Nanoscale* **2019**, *11*, 8855–8863. [CrossRef]
21. Zhang, C.; Du, X.; Wang, Y.; Han, X.; Zhang, X. $NiSe_2$@NixSy nanorod on nickel foam as efficient bifunctional electrocatalyst for overall water splitting. *Int. J. Hydrogen Energy* **2021**, *46*, 34713–34726. [CrossRef]
22. Tang, T.; Jiang, W.J.; Niu, S.; Liu, N.; Luo, H.; Chen, Y.Y.; Jin, S.F.; Gao, F.; Wan, L.J.; Hu, J.S. Electronic and morphological dual modulation of cobalt carbonate hydroxides by Mn doping toward highly efficient and stable bifunctional electrocatalysts for overall water splitting. *J. Am. Chem. Soc.* **2017**, *139*, 8320–8328. [CrossRef]
23. Alegre, C.; Busacca, C.; Di Blasi, A.; Di Blasi, O.; Aricò, A.; Antonucci, V.; Baglio, V. Toward more efficient and stable bifunctional electrocatalysts for oxygen electrodes using FeCo2O4/carbon nanofiber prepared by electrospinning. *Mater. Today Energy* **2020**, *18*, 100508. [CrossRef]
24. Sun, Y.Y.; Zhang, X.Y.; Tang, J.; Li, X.; Fu, H.Q.; Xu, H.G.; Mao, F.; Liu, P.F.; Yang, G.H. Amorphous oxysulfide reconstructed from spinel $NiCo_2S_4$ for efficient water oxidation. *Small* **2023**, *19*, 2207965. [CrossRef] [PubMed]
25. Tang, Q.; Jiang, D.E. Mechanism of hydrogen evolution reaction on 1T-MoS_2 from first principles. *ACS Catal.* **2016**, *6*, 4953–4961. [CrossRef]
26. Lukowski, M.A.; Daniel, S.A.; Meng, F.; Forticaux, A.; Li, L.; Jin, S. Enhanced hydrogen evolution catalysis from chemically exfoliated metallic MoS_2 nanosheets. *J. Am. Chem. Soc.* **2013**, *135*, 10274–10277. [CrossRef]
27. Qu, J.; Li, Y.; Li, F.; Li, T.; Wang, X.; Yin, Y.; Ma, L.; Schmidt, O.G.; Zhu, F. Direct thermal enhancement of hydrogen evolution reaction of on-chip monolayer MoS_2. *ACS Nano* **2022**, *16*, 2921–2927. [CrossRef]
28. Li, Z.; Hu, M.; Wang, P.; Liu, J.; Li, C. Heterojunction catalyst in electrocatalytic water splitting. *Coord. Chem. Rev.* **2021**, *439*, 213953. [CrossRef]
29. Ma, N.; Chen, G.; Zhu, Y.; Sun, H.; Dai, J.; Chu, H.; Ran, R.; Zhou, W.; Cai, R.; Shao, Z. A self-assembled hetero-structured inverse-spinel and anti-perovskite nanocomposite for ultrafast water oxidation. *Small* **2020**, *16*, 2002089. [CrossRef]
30. Wang, Z.; Hong, P.; Peng, S.; Zou, T.; Yang, Y.; Xing, X.; Wang, Z.; Zhao, R.; Yan, Z.; Wang, Y. $Co(OH)_2$@$FeCo_2O_4$ as electrode material for high performance faradaic supercapacitor application. *Electrochim. Acta* **2019**, *299*, 312–319. [CrossRef]
31. Li, S.; Wang, Y.; Sun, J.; Xu1, C.; Chen, H. Simple preparation of porous $FeCo_2O_4$ microspheres and nanosheets for advanced asymmetric supercapacitors. *ACS Appl. Energy Mater.* **2020**, *3*, 11307–11317. [CrossRef]
32. He, X.; Zhao, Y.; Chen, R.; Zhang, H.; Liu, J.; Liu, Q.; Song, D.; Li, R.; Wang, J. Hierarchical $FeCo_2O_4$@polypyrrole core/shell nanowires on carbon cloth for high-performance flexible all-solid-state asymmetric supercapacitors. *ACS Sustain. Chem. Eng.* **2018**, *6*, 14945–14954. [CrossRef]

33. Huang, C.; Liu, H.; Sun, C.; Wang, P.; Tian, Z.; Cheng, H.; Huang, S.; Yang, X.; Wang, M.; Liu, Z. Peroxymonosulfate activation by graphene oxide-supported 3D-MoS_2/$FeCo_2O_4$ sponge for highly efficient organic pollutants degradation. *Environ. Pollut.* **2023**, *325*, 121391. [CrossRef]
34. Ghosal Chowdhury, M.; Sahoo, L.; Maity, S.; Bain, D.; Gautam, U.K.; Patra, A. Silver nanocluster/MoS_2 heterostructures for hydrogen evolution. *ACS Appl. Nano Mater.* **2022**, *5*, 7132–7141. [CrossRef]
35. Su, C.; Xu, S.; Zhang, L.; Chen, X.; Guan, G.; Hu, N.; Su, Y.; Zhou, Z.; Wei, H.; Yang, Z. Hierarchical $CoNi_2S_4$ nanosheet/nanotube array structure on carbon fiber cloth for high-performance hybrid supercapacitors. *Electrochim. Acta* **2019**, *305*, 81–89. [CrossRef]
36. He, X.; Li, R.; Liu, J.; Liu, Q.; Chen, R.; Song, D.; Wang, J. Hierarchical $FeCo_2O_4$@NiCo layered double hydroxide core/shell nanowires for high performance flexible all-solid-state asymmetric supercapacitors. *Chem. Eng. J.* **2018**, *334*, 1573–1583. [CrossRef]
37. Zhou, R.; Zhao, J.; Shen, N.; Ma, T.; Su, Y.; Ren, H. Efficient degradation of 2,4-dichlorophenol in aqueous solution by peroxymonosulfate activated with magnetic spinel $FeCo_2O_4$ nanoparticles. *Chemosphere* **2018**, *197*, 670–679. [CrossRef] [PubMed]
38. Wang, Y.; Yan, D.; El Hankari, S.; Zou, Y.; Wang, S. Recent progress on layered double hydroxides and their derivatives for electrocatalytic water splitting. *Adv. Sci.* **2018**, *5*, 1800064. [CrossRef] [PubMed]
39. Zhou, G.; Shan, Y.; Wang, L.; Hu, Y.; Guo, J.; Hu, F.; Shen, J.; Gu, Y.; Cui, J.; Liu, L.; et al. Photoinduced semiconductor-metal transition in ultrathin troilite FeS nanosheets to trigger efficient hydrogen evolution. *Nat. Commun.* **2019**, *10*, 399. [CrossRef] [PubMed]
40. Tao, B.; Yang, L.; Miao, F.; Zang, Y.; Chu, P.K. An MoS_2/$NiCo_2O_4$ composite supported on Ni foam as a bifunctional electrocatalyst for efficient overall water splitting. *J. Phys. Chem. Solids* **2021**, *150*, 109842. [CrossRef]